*Nano Research*
DOI 10.1007/s12274-015-0762-6
**Research Article**
ISSN 1998-0124
CN 11-5974/O4

# Strain-induced direct–indirect bandgap transition and phonon modulation in monolayer $WS_2$

Yanlong Wang[1,2,§], Chunxiao Cong[2,§], Weihuang Yang[1,2], Jingzhi Shang[2], Namphung Peimyoo[2], Yu Chen[2], Junyong Kang[3], Jianpu Wang[1,4], Wei Huang[1,4,5] (✉), and Ting Yu[2] (✉)

[1] *Nanyang Technological University–Nanjing Tech Center of Research and Development, Nanjing Tech University, Nanjing 211816, China*
[2] *Division of Physics and Applied Physics, School of Physical and Mathematical Sciences, Nanyang Technological University, 637371, Singapore*
[3] *Fujian Key Laboratory of Semiconductor Materials and Applications, Department of Physics, Xiamen University, Xiamen 361005, China*
[4] *Key Laboratory of Flexible Electronics (KLOFE) and Institute of Advanced Materials (IAM), Jiangsu National Synergetic Center for Advanced Materials (SICAM), Nanjing Tech University (NanjingTech), Nanjing 211816, China*
[5] *Key Laboratory for Organic Electronics & Information Displays (KLOEID) and Institute of Advanced Materials (IAM), Nanjing University of Posts & Telecommunications, 9 Wenyuan Road, Nanjing 210046, China*
[§] *These authors contributed equally to this work.*

**Received:** 12 January 2015
**Revised:** 25 February 2015
**Accepted:** 4 March 2015



## KEYWORDS

monolayer $WS_2$,
strain,
light-emission tuning,
indirect transition,
trion,
crystallographic orientation

## ABSTRACT

*In situ* strain photoluminescence (PL) and Raman spectroscopy have been employed to exploit the evolutions of the electronic band structure and lattice vibrational responses of chemical vapor deposition (CVD)-grown monolayer tungsten disulphide ($WS_2$) under uniaxial tensile strain. Observable broadening and appearance of an extra small feature at the longer-wavelength side shoulder of the PL peak occur under 2.5% strain, which could indicate the direct–indirect bandgap transition and is further confirmed by our density-functional-theory calculations. As the strain increases further, the spectral weight of the indirect transition gradually increases. Over the entire strain range, with the increase of the strain, the light emissions corresponding to each optical transition, such as the direct bandgap transition (K–K) and indirect bandgap transition (Γ–K, $\geqslant$2.5%), exhibit a monotonous linear redshift. In addition, the binding energy of the indirect transition is found to be larger than that of the direct transition, and the slight lowering of the trion dissociation energy with increasing strain is observed. The strain was used to modulate not only the electronic band structure but also the lattice vibrations. The softening and splitting of the in-plane E′ mode is observed under uniaxial tensile strain, and polarization-dependent Raman spectroscopy confirms the observed zigzag-oriented edge of $WS_2$ grown by CVD in previous studies. These findings enrich our understanding of the strained states of monolayer transition-metal dichalcogenide (TMD) materials and lay a foundation for developing applications exploiting their strain-dependent optical properties, including the strain detection and light-emission modulation of such emerging two-dimensional TMDs.

Address correspondence to Wei Huang, wei-huang@njupt.edu.cn; Ting Yu, yuting@ntu.edu.sg

## 1 Introduction

Transition-metal dichalcogenides (TMDs) are generally expressed as $MX_2$, where M symbolizes a transition-metal element, and X represents a chalcogen atom. Bulk TMDs have a layered structure with each layer comprising two chalcogenide-atom planes and one transition-metal atom sub layer situated between them. The most common stacking polytype is 2H, with a trigonal prism unit that comprises the center metal atom and the six nearest chalcogen atoms [1, 2]. TMDs have long been known to possess a remarkable variety of important physical and chemical properties [3, 4]. Recently, as the fabrication and characterization techniques have matured, two-dimensional (2D) TMDs have drawn widespread research interest. Consequently, many extraordinary results have been obtained, such as the thinning-induced bandgap type transition [5–7], valley confinement due to inversion asymmetry [8, 9], a high effective Young's modulus [10], and nonblinking photon emission [11].

Strain engineering plays a key role in tuning the properties of 2D materials. The effects of strain on monolayer graphene have been widely studied. The lattice vibration, the magnetism, and even the electronic band structures of graphene can be remarkably influenced by applying strain [12–18]. Owing to their as-born bandgap and extremely high breaking strength [10, 19], atomically thin TMDs provide a good opportunity to examine strain effects on 2D materials. Phonon softening [20, 21], crystal-orientation determination [20], bandgap narrowing [22, 23], valley polarization decrease [24], and giant valley drift [25] have been reported under tensile strain in monolayer $MoS_2$. However, the influences of strain on the direct-bandgap feature, e.g., a direct–indirect bandgap transition under strain predicted by theoretical calculations [26–29], have not been systematically studied by any experimental approach, even though the direct-bandgap feature is the most interesting and important property of 2D TMDs. Moreover, the effects of strain on the trion feature, which was recently assigned in several monolayer TMDs [9, 30–32] have not been experimentally investigated, to our knowledge. Furthermore, the edges of CVD-grown 2D TMDs are revealed by transmission electron microscopy to have zigzag termination. They are not atomically sharp, and further investigation is needed to accurately identify the edge orientation [33–35], which is important for determining the properties of TMD materials [36]. 2D tungsten disulphide ($WS_2$), a type of TMD material, has been demonstrated to have potential for optoelectronics, photonics, and nanoelectronics, both in independent forms and heterostructures [37–40]. The CVD method was employed to successfully grow high-quality monolayer $WS_2$ in a large area, as discussed in our recent reports [11, 33]. A study of the strain-dependent properties could yield further insight into the potential applications of this material, especially the flexibility-related ones [41]. However, experimental investigations of the effects of the strain on the light emission and lattice vibration for 2D $WS_2$ are still lacking, in stark contrast to those for 2D $MoS_2$ [20–24]. In this paper, we report the tunable light emission and lattice vibration of CVD-grown monolayer $WS_2$ under uniaxial tensile strain. Both the bandgap-energy tuning and direct–indirect transition induced by the strain are revealed by photoluminescence (PL) spectra. Furthermore, the trion and phonon behaviors influenced by the strain are discussed. Finally, the polarization-dependent intensities of the split $E'^{+}$ and $E'^{-}$ modes are analyzed to determine the crystallographic orientation of the CVD-grown $WS_2$.

## 2 Experimental

Monolayer $WS_2$ samples were grown by CVD on a $SiO_2$/Si substrate and then transferred to a flexible polyethylene terephthalate (PET) substrate for strained Raman and PL measurements.

Growth and transfer: The CVD method [33] was employed to grow the monolayer $WS_2$. The desired areas were located using corresponding optical and fluorescence images taken by an optical microscope (BX 51). Then, the grown samples were transferred to a PET substrate by the improved method proposed by Li et al. [60].

Strain application: The samples were mounted on a strain stage with the desired areas in the middle of the stage gap and controllably elongated to apply uniaxial tensile strain.

Optical characterization: Raman spectra were collected by a Raman system (Witec CRM200) with 1800- and 2400-lines/mm grating under 457- and 488-nm excitation lasers, respectively. PL measurements were conducted in the same Witec system with 150-lines/mm grating under both 457- and 532-nm laser lines. The laser spot was ~500 nm in diameter. The PL spectra before and after the transfer process were measured under the same conditions. The Raman spectrum of the monolayer $WS_2$ transferred to the PET substrate was measured with longer integration time and higher power than that of the as-grown one, for better comparison. In each strain-loading process, at least three different points were examined, to ensure that the observed spectrum change was typical. The Raman and PL measurements were performed under the same conditions for different strains, with a low laser power to avoid damage to the samples. Under some specific strain strengths, several spectra were taken for the same spot and compared to confirm the validity of measurement results.

## 3 Calculation methods

Electronic-structure calculations for the unstrained and strained $WS_2$ monolayer based on the density functional theory (DFT) were performed using the projector-augmented wave pseudopotentials method with a plane-wave basis set, as implemented in the Vienna *ab initio* simulation package (VASP) code [61–63]. The plane-wave cutoff energy was 500 eV, and the exchange-correlation functional was treated within the local density approximation (LDA) according to the Ceperlay Alder (CA) parameterization. The 1H-$WS_2$ monolayer was modeled by a 1 × 1 unit cell containing 3 atoms. A vacuum spacing larger than 22 Å was introduced to hinder the interaction between periodic replicas along the *c* axis, effectively isolating the monolayer structure. The convergence condition for the energy was chosen as $10^{-6}$ eV, and the structures were relaxed until the forces on each atom were less than 0.01 eV/Å. The Monkhorst–Pack scheme was used to sample the Brillouin zone. To obtain the unstrained configuration, the atomic positions and lattice vectors were fully relaxed with a mesh of 15 × 15 × 1, and the optimized (relaxed) coordinates were then used for self-consistent and density-of-state (DOS) calculations with the mesh of *k* space increased to 25 × 25 × 1. The band structures were calculated along the high-symmetry points using the path Γ–M–K–Γ. Because the uniaxial strain effects on the band structure (especially the band-edge parts) of monolayer TMD materials are nearly direction-independent [23, 24, 26], we only considered the strain in the [010] direction. The lattice vector in this direction increased with the strain strength, whereas those in the other two directions were kept constant.

## 4 Results and discussion

To effectively apply uniaxial strain to the monolayer $WS_2$, the as-grown CVD $WS_2$ thin layers on the $SiO_2$/Si substrate were transferred onto a flexible substrate such as PET (see the discussion and Fig. S1 in the Electronic Supplementary Material (ESM) for details). As shown in Figs. 1(a) and 1(b), optical images of the monolayer $WS_2$ before and after the transfer reveal that the transferred sample maintained its original perfect triangular shape. Raman spectroscopy—a unique and powerful tool for investigating the layer number [42–44], stacking order [45–47], local oxidation [48], and doping effects [49, 50]—was employed with a 457-nm excitation laser line to characterize the samples before and after the transfer. As shown in Fig. 1(c), under this excitation condition, one second-order zone-edge phonon mode (2LA(M), 347 $cm^{-1}$) and two zone-center modes (E′, 357 $cm^{-1}$ and $A_1'$, 417 $cm^{-1}$) dominated in the range of 300–480 $cm^{-1}$ [51]. No obvious spectral change is observed, confirming that the transferred sample maintained its quality.

Benefitting from a direct bandgap, monolayer TMDs typically possess strong PL emissions. Our CVD-grown monolayer $WS_2$ generally exhibited a strong and symmetric peak [11, 33]. As shown in Fig. 1(d), peak splitting clearly occurred after the transfer process. Considering that the transfer process may cause unintentional doping to the monolayer $WS_2$, we attribute the two split peaks to the neutral exciton (higher energy) and charged exciton or trion (lower energy), respectively. Similar excitonic-emission features were previously observed in $WS_2$ and other

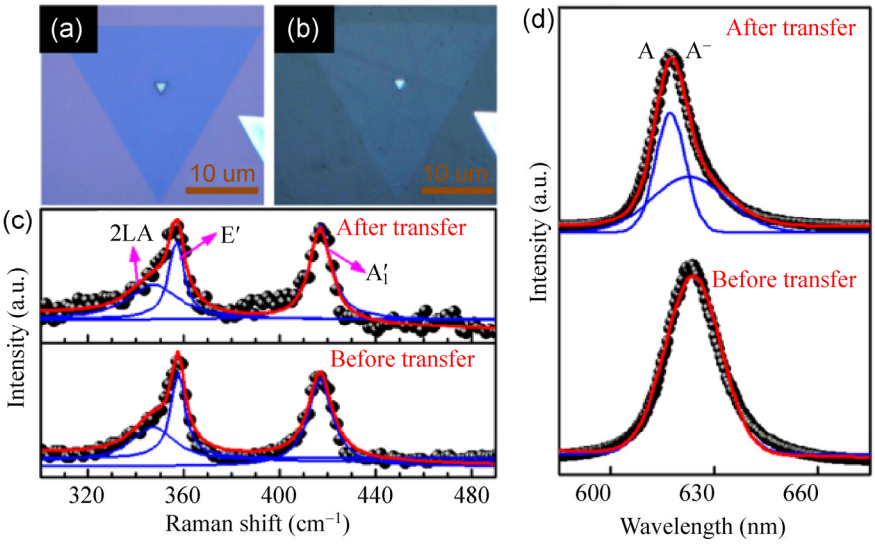


**Figure 1** (a) and (b) Optical images of CVD-grown monolayer $WS_2$ on (a) $SiO_2$/Si substrate and (b) PET substrate after transfer process. (c) Raman and (d) PL spectra of monolayer $WS_2$ before and after transfer, with fitted curves.

2D TMDs [9, 30–32]. Such excitonic emissions originate from the direct transition at the K point in the Brillouin zone [34], and there is a switch between the neutral exciton (A) and trion ($A^-$ or $A^+$ depending on extra carrier type) at different Fermi levels [9, 30–32]. In our previous studies, CVD-grown $WS_2$ exhibited an n-type doping property [11]. The excess of electrons in such n-type $WS_2$ could facilitate the formation of negatively charged excitons ($A^-$). For the transferred samples, the spectral-weight transformation from $A^-$ to A in the PL spectra is caused by the decrement of the n-type doping level due to the molecules that were trapped during the transfer process. The molecular-doping effects on the light emissions of the $WS_2$ monolayer were discussed in our previous report [52].

To better understand the observed strain-dependent light-emission behaviors, we calculated the band structure of monolayer $WS_2$ under different uniaxial strains using the DFT method. Figure 2 shows the results (see the Calculation methods for details). One remarkable change in the band structure induced by applying uniaxial tensile strain is the direct–indirect bandgap transition, which was theoretically predicted for other monolayer TMD materials [23, 25, 26, 28, 29]. As shown in Fig. 2(a), in the unstrained state, both the valence-band maximum (VBM) and conduction-band minimum (CBM) are located at the point K. As the strain increases, the energy difference between the local maxima of the K and Γ points in the valence band (VB) decreases, and the maxima are nearly degenerate under 2.4% strain (Fig. 2(b)). A uniaxial strain of 2.6% can move the VBM of monolayer $WS_2$ from K to Γ while keeping the CBM unchanged, yielding the narrowest gap between the transition from Γ to K, as shown in Fig. 2(c). With the continuous increase of the strain, the indirect-bandgap feature becomes increasingly obvious (see the band structure with 3.8% strain in Fig. 2(d)). In addition, the zoomed-in view of the band structure around K (inset of Fig. 2(d)) shows that the strain can move the local VBM and CBM slightly away from K. This phenomenon, called the "valley drift," was recently observed in uniaxially strained monolayer $MoS_2$ [25] and will be studied in detail in the future.

To further investigate the strain-modulated electronic band structures revealed by our DFT calculation, detailed *in situ* strain PL spectra measurements are conducted. Figure 3(a) shows the evolution of the PL spectra in the monolayer $WS_2$ as a function of the uniaxial tensile strain. As the strain increased from 0 to 2.2%, there was an obvious redshift in the PL emission, while the line shape remained unchanged, which is similar to previous observations for strained monolayer $MoS_2$ [22, 24]. The broadening of the PL peak is observed under 2.5% strain (see Fig. S2 in the ESM), after which the PL spectrum continues to

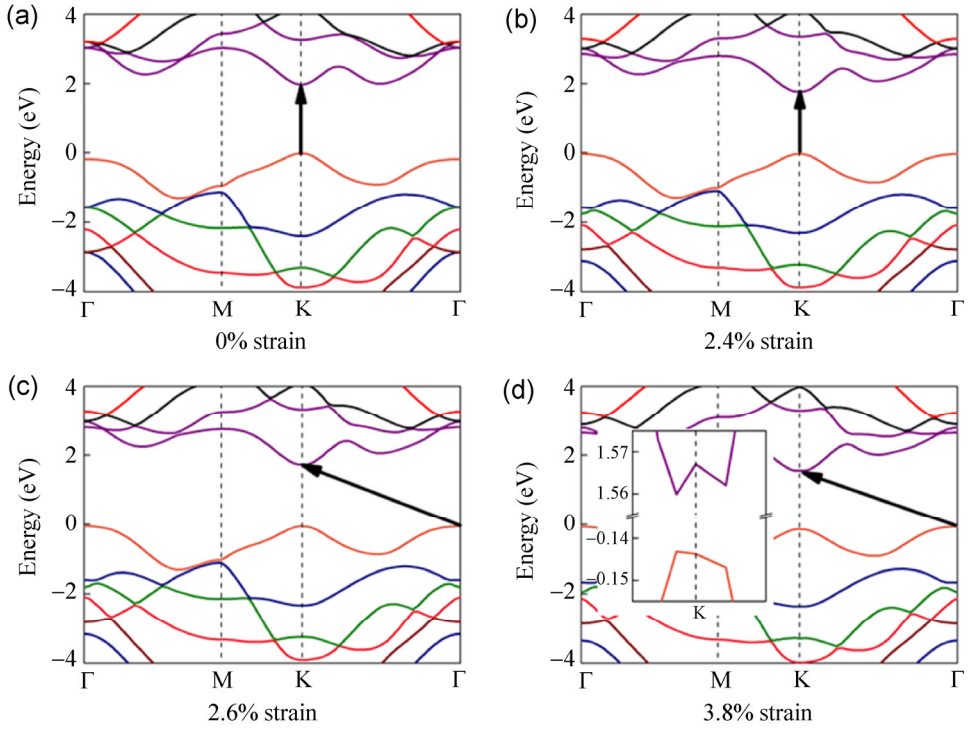


**Figure 2** Calculated band structure for monolayer $WS_2$ under (a) 0%, (b) 2.4%, (c) 2.6%, and (d) 3.8% uniaxial strain. Inset: zoomed-in band structure near CBM and VBM around point K.

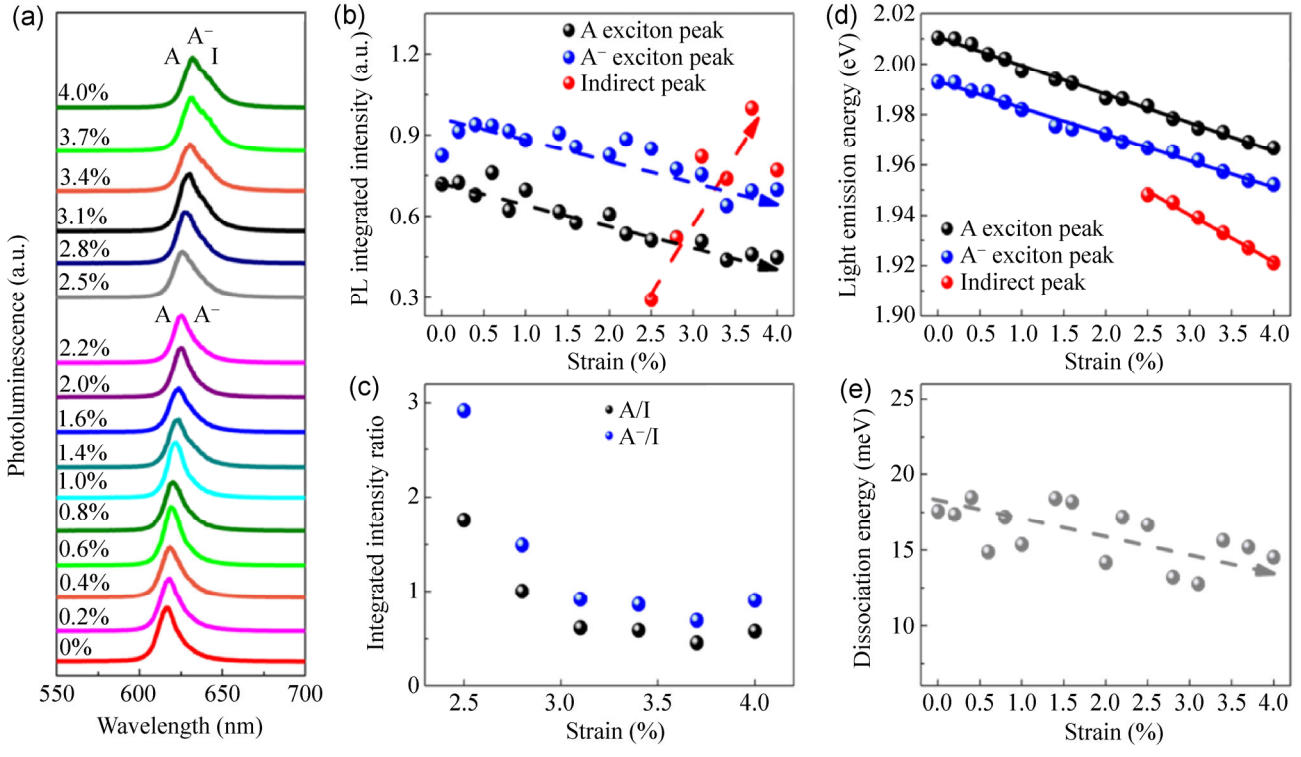


**Figure 3** (a) PL spectra, fitted light-emission (b) integrated intensities and (d) energies of A, $A^-$, and I peaks for CVD monolayer $WS_2$ as a function of uniaxial strain under 532-nm laser line. Intensities of all peaks are normalized by I-peak intensity under 3.7% strain, which is the largest of sub peaks in measured strain range. (c) and (e) show intensity ratios of direct–indirect transition peak and position–distance trend of A and $A^-$ peaks with increasing strain, respectively. Dashed lines in (b) and (e) serve as guides for corresponding trend under strain; solid lines in (c) show linear fit.

broaden and entirely redshifts with increasing strain. Considering that our DFT observation of the direct–indirect bandgap transition occurs under ca. 2.6%, such broadening, especially at the longer wavelength tail, may arise from the extra contribution of the light emission from the indirect bandgap (Γ–K). To test this hypothesis, we fitted the PL spectra with strain below 2.5% by two Gaussian peaks and fitted the PL spectra under strain above 2.5% by three Gaussian peaks. This strategy yielded excellent fittings, as demonstrated by the representative spectra shown in Fig. S2 in the ESM. Notably, the newly appearing peak under strain no less than 2.5% (expressed as I, represents indirect hereinafter) is always broader than the other two, which agrees with the feature of the indirect-gap emission peak observed in few-layer $WS_2$ [7, 34]. This broadening is partly attributed to the phonon that participates in the recombination process of the indirect transition to satisfy momentum conservation by providing the appropriate momentum [53]. As shown in Fig. 3(b), the I peak intensity tends to increase with the strain, in contrast to those of the A and $A^-$ peaks. The simultaneous reduction of the two intensity ratios (A/I and $A^-$/I) (see Fig. 3(c)) yields a direct–indirect spectral-weight conversion with increasing strain, as a result of the faster strain-induced energy narrowing rate of the indirect transition compared with that of the direct one. The fitted light-emission energies as a function of the strain are shown in Fig. 3(d). In addition to the expected linear redshift of the A exciton peak with the strain (–0.0113 eV/%), which is also observed in monolayer $MoS_2$ [22–24], the I peak is linearly redshifted at a higher rate of –0.0187 eV/%. Notably, under 2.5% strain, the energy of the I peak is 35 meV smaller than that of the A peak. This contrasts the expected observation of the approximate energy degeneracy of these two transitions near the critical strain to transform the bandgap type. We attribute the discrepancy to the larger binding energy of the indirect transition compared with that of the direct one. The light-emission energy measured by PL spectroscopy represents the fundamental bandgap subtracted by the binding energy of the corresponding transition. The exciton binding energy is linearly dependent on the effective exciton mass [54], and the latter is jointly determined by the effective electron and hole mass at the band edge according to the expression $\mu_{ex} = m_e m_h/(m_e+m_h)$. Because the direct and indirect transitions have the same effective electron mass, the considerably larger hole mass at Γ than at K [55] leads to stronger binding for the indirect transition. This different binding energy and the near-degenerate fundamental energy gap cause the lower energy of the I peak, which makes the peaks distinguishable in the PL spectrum. Furthermore, the trion-dissociation-energy evolution under strain can be estimated by extracting the strain-dependent energy distances of the A and $A^-$ peaks. A slightly decreasing trend is observed, as shown in Fig. 3(e). The decrease in the trion dissociation energy under increasing tensile strain is attributed to the changes in the effective exciton mass and polarizability caused by varying strain [55, 56]. Increasing the strain could reduce the effective exciton mass while enlarging the polarizability [55]. The smaller effective exciton mass and larger polarizability cause the reduction of the trion dissociation energy [56]. To confirm that the indirect transition peak does contribute to the observed PL spectra, in Fig. S3 in the ESM, we present results obtained by fitting all the PL spectra under strain with two Gaussian peaks. The fitted intensity of the $A^-$ peak increases remarkably in the high-strain region, where the shortest transition is indirect, and the dissociation energy decreases slightly with increasing strain. This does not agree with the expected strain-induced light-emission change, as previously discussed, and provides additional evidence for the assignment of the I peak in the PL spectra under high strain.

In addition to the electronic band structure, the lattice vibration of such 2D systems is highly sensitive to strain. Strain-dependent Raman spectra for the monolayer $WS_2$ are displayed in Fig. 4(a). Here, we notice the extreme sensitivity of the E′ mode to the strain. The strain-induced redshift and splitting of this mode under high strain are clearly observed. In contrast, the out-of-plane $A_1'$ mode is more inert to the in-plane strain. As schematically illustrated in Fig. 4(b), the E′ mode involves in-plane opposite displacements of W and S atoms, whereas the $A_1'$ mode merely corresponds to the vibrations of S atoms out-of-phase perpendicular to the plane [2]. We previously performed an analysis of the different responses of these

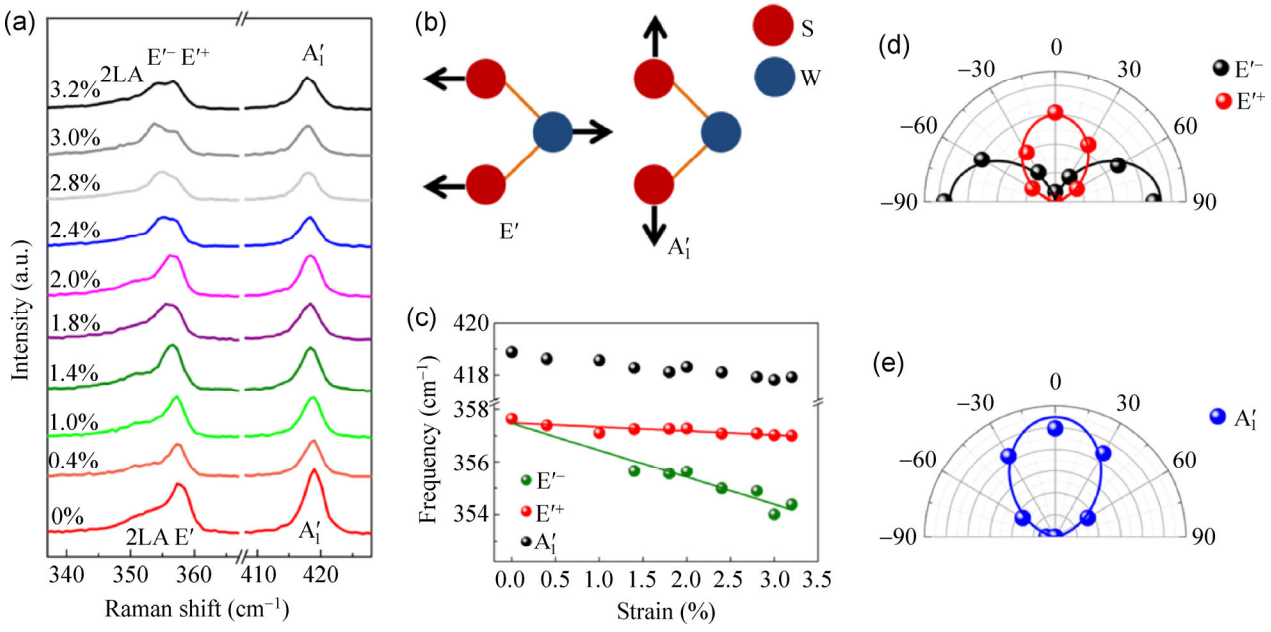


**Figure 4** (a) Raman spectra of monolayer CVD $WS_2$ with increasing strain under 488-nm laser line. (b) Schematic illustration of atomic displacements for two first-order phonon modes. (c) Fitted phonon frequencies of E′ and $A_1'$ modes of monolayer $WS_2$ as a function of uniaxial strain. (d) and (e) show polar maps of fitted Raman intensities of $E'^{+}$, $E'^{-}$, and $A_1'$ modes as a function of angle $\phi$ under uniaxial strain of 3.2%.

two phonon modes to the uniaxial strain in monolayer $MoS_2$ based on their distinct atomic displacements and symmetry breaking [20]. This was later verified by Conley et al. [23]. To accurately reveal the behaviors of the phonon modes under strain, multiple Lorentzian functions were adopted to fit the Raman spectra under different strains. As clearly indicated by the fitted phonon frequencies with respect to the strain (Fig. 4(c)), the double degenerate in-plane E′ mode linearly softens under small strain and then splits under 1.4% strain, after which both the $E'^{+}$ and $E'^{-}$ peaks have a linear relationship with the strain value. The $A_1'$ mode maintained its single Lorentz shape throughout the applied-strain range, as expected. At high strains, the $A_1'$ mode underwent a slight redshift of less than 0.4 $cm^{-1}$, i.e., 2%–3.2%. This is slightly surprising, as this mode should be insensitive to in-plane strain. We attribute this redshift to the laser-induced heating, which becomes increasingly significant as the sample is subjected to laser shining instead of strain. Because the $A_1'$ mode is reported to be more susceptible to laser-induced heating [57] and temperature [58, 59] than the E′ mode for monolayer TMDs, its unexpected redshift under strain is understandable.

We previously demonstrated that polarization-dependent Raman spectroscopy is a unique and efficient way to determine the crystal orientation of mechanically exfoliated monolayer $MoS_2$ under uniaxial strain [20]. In the present study, we adopted this technique to identify the edge and crystal orientation of our CVD-grown monolayer $WS_2$. Figure S4(a) in the ESM shows the measured polarization-dependent Raman spectra for the as-transferred CVD-grown monolayer $WS_2$ under zero strain. In our polarization configuration, the incident light is constantly polarized along the horizontal direction, and the scattered-light polarization is chosen with an angle $\phi$, corresponding to the horizontal direction, by a linear polarizer. The fitted results (Fig. S4(b) in the ESM) clearly show that the intensity of the E′ mode has a $\cos^2\phi$ dependence, whereas that of the $A_1'$ mode is insensitive to the polarization angle. This is well explained according to the different Raman tensors of the two modes [20]. A schematic diagram of the polarization geometry for our polar-dependent Raman measurements under uniaxial strain is displayed in Fig. S5(a) in the ESM. The zigzag direction is assumed to have the angle $\theta$ relative to the $x$-axis. Strain was applied in the horizontal

direction, and the incident-light polarization was fixed in the $x$-axis direction, yielding $\psi = 0°$. The polarization of the scattered light was selected by an analyzer and tuned from –90° to 90° relative to the strain direction (the angle $\phi$) with steps of 30°. We fitted the obtained Raman spectra of the monolayer $WS_2$ as a function of $\phi$ under a uniaxial strain of 3.2% (see Fig. S5(b) in the ESM). The polar-angle dependence of the $E'^{+}$, $E'^{-}$, and $A_1'$ peaks are plotted in Figs. 4(d) and 4(e). The intensity of the $A_1'$ mode is proportional to $\cos^2\phi$, similarly to the non-strain case, as this out-of-plane mode is seldom affected by in-plane strain [20]. In contrast, the intensities of the $E'^{+}$ and $E'^{-}$ modes have $\cos^2\phi$ and $\sin^2\phi$ dependence, respectively. Because the polarization-dependent intensities of these two split $E'^{+}$ and $E'^{-}$ modes in our configuration are theoretically proportional to $\cos^2(\phi+3\theta)$ and $\sin^2(\phi+3\theta)$, respectively [20], the $\theta$ value is obtained as 0°. Thus, the zigzag direction of our CVD-grown monolayer $WS_2$ is determined to be along the horizontal axis, which happens to overlap with one of the triangle edges, as shown in Fig. 1(b). This confirms the previous observations that the CVD-grown $WS_2$ edge is zigzag-terminated [33, 34].

## 5 Conclusions

We studied the strain-dependent light emission and lattice vibration of CVD-grown monolayer $WS_2$ and experimentally demonstrated the tuning of different optical transition energies and their relative spectral weights by applying uniaxial strain. This tunable optical property is attributed to the strain-induced direct–indirect bandgap transition and was confirmed by DFT calculations. We also showed that the uniaxial tensile strain can decrease the trion dissociation energy and soften the in-plane E′ phonon mode, followed by lifting its two-fold degeneracy. The difference in the polarization dependence between the split $E'^{+}$ and $E'^{-}$ modes can be used to efficiently identify the crystal orientation and confirm the zigzag-type edge of CVD-grown monolayer $WS_2$. These findings extend previous studies of strained TMDs, corroborating theoretical predictions regarding the effects of strain on the band structural evolution and elucidating strain-dependent trion behaviors. The observed sensitivity of the light emission to strain in monolayer $WS_2$ caused by the strain-induced bandgap type and energy change further indicates the potential of this atomically thin TMD material for various applications, such as strain detection and optoelectronics.

## Acknowledgements

This work is supported by the Singapore National Research Foundation NRF RF Award No. NRFRF2010-07, MOE Tier 2 MOE2012-T2-2-049, A*Star SERC PSF grant No. 1321202101, and MOE Tier 1 MOE2013–T1–2–235. W. Huang acknowledges the support of the National Basic Research Program of China (973 Program) (No. 2015CB932200), the National Natural Science Foundation of China (NSFC) (Grant Nos. 21144004, 20974046, 21101095, 21003076, 20774043, 51173081, 50428303, 61136003, and 50428303), the Ministry of Education of China (No. IRT1148), the NSF of Jiangsu Province (Grant Nos. SBK201122680, 11KJB510017, BK2008053, 11KJB510017, BK2009025, 10KJB510013, and BZ2010043), and NUPT (Nos. NY210030 and NY211022). J. P. Wang is grateful for the NSFC (No. 11474164), NSF of Jiangsu province (No. BK20131413), and the Jiangsu Specially-Appointed Professor program. Y. L. Wang thanks Luqing Wang, Dr. Xiaolong Zou, and Dr. Alex Kutana for the constructive discussion.

**Electronic Supplementary Material**: Supplementary material (layer-thickness determination, PL spectra with fitted curve, results obtained by fitting all PL spectra under strain with two Gaussian peaks, polarization geometry, polarization-dependent Raman intensity under zero strain, and polar-dependent Raman spectra under 3.2% strain) is available in the online version of this article at http://dx.doi.org/10.1007/s12274-015-0762-6.

## References

[1] Bromley, R. A.; Yoffe, A. D.; Murray, R. The band structures of some transition metal dichalcogenides. III. Group VIA: Trigonal prism materials. *J. Phys. C: Solid State Phys.* **2001**, *5*, 759–778.

[2] Lucovsky, G.; White, R. M.; Benda, J. A.; Revelli, J. F.

Infrared-reflectance spectra of layered group-IV and group-VI transition-metal dichalcogenides. *Phys. Rev. B* **1973**, *7*, 3859–3870.

[3] Wilson, J. A.; Yoffe, A. D. The transition metal dichalcogenides discussion and interpretation of the observed optical, electrical and structural properties. *Adv. Phys.* **1969**, *18*, 193–335.

[4] Fortin, E.; Sears, W. M. Photovoltaic effect and optical absorption in $MoS_2$. *J. Phys. Chem. Solids* **1982**, *43*, 881–884.

[5] Mak, K. F.; Lee, C.; Hone, J.; Shan, J.; Heinz, T. F. Atomically thin $MoS_2$: A new direct-gap semiconductor. *Phys. Rev. Lett.* **2010**, *105*, 136805.

[6] Splendiani, A.; Sun, L.; Zhang, Y. B.; Li, T. S.; Kim, J.; Chim, C. Y.; Galli, G.; Wang, F. Emerging photoluminescence in monolayer $MoS_2$. *Nano Lett.* **2010**, *10*, 1271–1275.

[7] Zhao, W. J.; Ghorannevis, Z.; Chu, L. Q.; Toh, M. L.; Kloc, C.; Tan, P. H.; Eda, G. Evolution of electronic structure in atomically thin sheets of $WS_2$ and $WSe_2$. *ACS Nano* **2012**, *7*, 791–797.

[8] Mak, K. F.; He, K. L.; Shan, J.; Heinz, T. F. Control of valley polarization in monolayer $MoS_2$ by optical helicity. *Nat. Nano.* **2012**, *7*, 494–498.

[9] Jones, A. M.; Yu, H. Y.; Ghimire, N. J.; Wu, S. F.; Aivazian, G.; Ross, J. S.; Zhao, B.; Yan, J. Q.; Mandrus, D. G.; Xiao, D. et al. Optical generation of excitonic valley coherence in monolayer $WSe_2$. *Nat. Nanotechnol.* **2013**, *8*, 634–638.

[10] Bertolazzi, S.; Brivio, J.; Kis, A. Stretching and breaking of ultrathin $MoS_2$. *ACS Nano* **2011**, *5*, 9703–9709.

[11] Peimyoo, N.; Shang, J. Z.; Cong, C. X.; Shen, X. N.; Wu, X. Y.; Yeow, E. K. L.; Yu, T. Nonblinking, intense two-dimensional light emitter: Monolayer $WS_2$ triangles. *ACS Nano.* **2013**, *7*, 10985–10994.

[12] Yu, T.; Ni, Z. H.; Du, C. L.; You, Y. M.; Wang, Y. Y.; Shen, Z. X. Raman mapping investigation of graphene on transparent flexible substrate: The strain effect. *J. Phys. Chem. C* **2008**, *112*, 12602–12605.

[13] Ni, Z. H.; Yu, T.; Lu, Y. H.; Wang, Y. Y.; Feng, Y. P.; Shen, Z. X. Uniaxial strain on graphene: Raman spectroscopy study and band-gap opening. *ACS Nano* **2008**, *2*, 2301–2305.

[14] Huang, M. Y.; Yan, H. G.; Chen, C. Y.; Song, D. H.; Heinz, T. F.; Hone, J. Phonon softening and crystallographic orientation of strained graphene studied by Raman spectroscopy. *Proc. Natl. Acad. Sci. U.S.A.* **2009**, *106*, 7304–7308.

[15] Mohiuddin, T. M. G.; Lombardo, A.; Nair, R. R.; Bonetti, A.; Savini, G.; Jalil, R.; Bonini, N.; Basko, D. M.; Galiotis, C.; Marzari, N. et al. Uniaxial strain in graphene by Raman spectroscopy: G peak splitting, Grüneisen parameters, and sample orientation. *Phys. Rev. B* **2009**, *79*, 205433.

[16] Kou, L. Z.; Tang, C.; Guo, W. L.; Chen, C. F. Tunable magnetism in strained graphene with topological line defect. *ACS Nano* **2011**, *5*, 1012–1017.

[17] Huang, B.; Yu, J. J.; Wei, S. H. Strain control of magnetism in graphene decorated by transition-metal atoms. *Phys. Rev. B* **2011**, *84*, 075415.

[18] Pereira, V. M.; Castro Neto, A. H.; Peres, N. M. R. Tight-binding approach to uniaxial strain in graphene. *Phys. Rev. B* **2009**, *80*, 045401.

[19] Cooper, R. C.; Lee, C.; Marianetti, C. A.; Wei, X.; Hone, J.; Kysar, J. W. Nonlinear elastic behavior of two-dimensional molybdenum disulfide. *Phys. Rev. B* **2013**, *87*, 035423.

[20] Wang, Y. L.; Cong, C. X.; Qiu, C. Y.; Yu, T. Raman spectroscopy study of lattice vibration and crystallographic orientation of monolayer $MoS_2$ under uniaxial strain. *Small* **2013**, *9*, 2857–2861.

[21] Rice, C.; Young, R. J.; Zan, R.; Bangert, U.; Wolverson, D.; Georgiou, T.; Jalil, R.; Novoselov, K. S. Raman-scattering measurements and first-principles calculations of strain-induced phonon shifts in monolayer $MoS_2$. *Phys. Rev. B* **2013**, *87*, 081307.

[22] He, K. L.; Poole, C.; Mak, K. F.; Shan, J. Experimental demonstration of continuous electronic structure tuning via strain in atomically thin $MoS_2$. *Nano Lett.* **2013**, *13*, 2931–2936.

[23] Conley, H. J.; Wang, B.; Ziegler, J. I.; Haglund, R. F., Jr.; Pantelides, S. T.; Bolotin, K. I. Bandgap engineering of strained monolayer and bilayer $MoS_2$. *Nano Lett.* **2013**, *13*, 3626–3630.

[24] Zhu, C. R.; Wang, G.; Liu, B. L.; Marie, X.; Qiao, X. F.; Zhang, X.; Wu, X. X.; Fan, H.; Tan, P. H.; Amand, T. et al. Strain tuning of optical emission energy and polarization in monolayer and bilayer $MoS_2$. *Phys. Rev. B* **2013**, *88*, 121301.

[25] Zhang, Q. Y.; Cheng, Y. C.; Gan, L. Y.; Schwingenschlögl, U. Giant valley drifts in uniaxially strained monolayer $MoS_2$. *Phys. Rev. B* **2013**, *88*, 245447.

[26] Johari, P.; Shenoy, V. B. Tuning the electronic properties of semiconducting transition metal dichalcogenides by applying mechanical strains. *ACS Nano* **2012**, *6*, 5449–5456.

[27] Scalise, E.; Houssa, M.; Pourtois, G.; Afanas'ev, V. V.; Stesmans, A. Strain-induced semiconductor to metal transition in the two-dimensional honeycomb structure of $MoS_2$. *Nano Res.* **2011**, *5*, 43–48.

[28] Lu, P.; Wu, X. J.; Guo, W. L.; Zeng, X. C. Strain-dependent electronic and magnetic properties of $MoS_2$ monolayer, bilayer, nanoribbons and nanotubes. *Phys. Chem. Chem. Phys.* **2012**, *14*, 13035–13040.

[29] Kumar, A.; Ahluwalia, P. K. Mechanical strain dependent electronic and dielectric properties of two-dimensional honeycomb structures of $MoX_2$ (X = S, Se, Te). *Physica B* **2013**, *419*, 66–75.

[30] Ross, J. S.; Wu, S. F.; Yu, H. Y.; Ghimire, N. J.; Jones, A. M.; Aivazian, G.; Yan, J. Q.; Mandrus, D. G.; Xiao, D.; Yao, W. et al. Electrical control of neutral and charged excitons in a monolayer semiconductor. *Nat. Commun.* **2013**, *4*, 1474.

[31] Mitioglu, A. A.; Plochocka, P.; Jadczak, J. N.; Escoffier, W.; Rikken, G. L. J. A.; Kulyuk, L.; Maude, D. K. Optical manipulation of the exciton charge state in single-layer tungsten disulfide. *Phys. Rev. B* **2013**, *88*, 245403.

[32] Mak, K. F.; He, K. L.; Lee, C.; Lee, G. H.; Hone, J.; Heinz, T. F.; Shan, J. Tightly bound trions in monolayer $MoS_2$. *Nat. Mater.* **2013**, *12*, 207–211.

[33] Cong, C. X.; Shang, J. Z.; Wu, X.; Cao, B. C.; Peimyoo, N.; Qiu, C.; Sun, L. T.; Yu, T. Synthesis and optical properties of large-area single-crystalline 2D semiconductor $WS_2$ monolayer from chemical vapor deposition. *Adv. Opt. Mater.* **2014**, *2*, 131–136.

[34] Gutierrez, H. R.; Perea-Lopez, N.; Elias, A. L.; Berkdemir, A.; Wang, B.; Lv, R.; Lopez-Urias, F.; Crespi, V. H.; Terrones, H.; Terrones, M. Extraordinary room-temperature photoluminescence in triangular $WS_2$ monolayers. *Nano Lett.* **2013**, *13*, 3447–3454.

[35] van der Zande, A. M.; Huang, P. Y.; Chenet, D. A.; Berkelbach, T. C.; You, Y. M.; Lee, G. H.; Heinz, T. F.; Reichman, D. R.; Muller, D. A.; Hone, J. C. Grains and grain boundaries in highly crystalline monolayer molybdenum disulphide. *Nat. Mater.* **2013**, *12*, 554–561.

[36] Hsu, W. T.; Zhao, Z. A.; Li, L. J.; Chen, C. H.; Chiu, M. H.; Chang, P. S.; Chou, Y. C.; Chang, W. H. Second harmonic generation from artificially stacked transition metal dichalcogenide twisted bilayers. *ACS Nano* **2014**, *8*, 2951–2958.

[37] Perea-López, N.; Elías, A. L.; Berkdemir, A.; Castro-Beltran, A.; Gutiérrez, H. R.; Feng, S. M.; Lv, R. T.; Hayashi, T.; López-Urías, F.; Ghosh, S. et al. Photosensor device based on few-layered $WS_2$ films. *Adv. Funct. Mater.* **2013**, *23*, 5511–5517.

[38] Georgiou, T.; Jalil, R.; Belle, B. D.; Britnell, L.; Gorbachev, R. V.; Morozov, S. V.; Kim, Y. J.; Gholinia, A.; Haigh, S. J.; Makarovsky, O. et al. Vertical field-effect transistor based on graphene–$WS_2$ heterostructures for flexible and transparent electronics. *Nat. Nanotechnol.* **2013**, *8*, 100–103.

[39] Britnell, L.; Ribeiro, R. M.; Eckmann, A.; Jalil, R.; Belle, B. D.; Mishchenko, A.; Kim, Y. J.; Gorbachev, R. V.; Georgiou, T.; Morozov, S. V. et al. Strong light-matter interactions in heterostructures of atomically thin films. *Science* **2013**, *340*, 1311–1314.

[40] Jo, S.; Ubrig, N.; Berger, H.; Kuzmenko, A. B.; Morpurgo, A. F. Mono- and bilayer $WS_2$ light-emitting transistors. *Nano Lett.* **2014**, *14*, 2019–2025.

[41] Shi, H. L.; Pan, H.; Zhang, Y. W.; Yakobson, B. I. Quasiparticle band structures and optical properties of strained monolayer $MoS_2$ and $WS_2$. *Phys. Rev. B* **2013**, *87*, 155304.

[42] Lee, C.; Yan, H.; Brus, L. E.; Heinz, T. F.; Hone, J.; Ryu, S. Anomalous lattice vibrations of single- and few-layer $MoS_2$. *ACS Nano* **2010**, *4*, 2695–2700.

[43] Ferrari, A. C.; Meyer, J. C.; Scardaci, V.; Casiraghi, C.; Lazzeri, M.; Mauri, F.; Piscanec, S.; Jiang, D.; Novoselov, K. S.; Roth, S. et al. Raman spectrum of graphene and graphene layers. *Phys. Rev. Lett.* **2006**, *97*, 187401.

[44] Li, S. L.; Miyazaki, H.; Song, H.; Kuramochi, H.; Nakaharai, S.; Tsukagoshi, K. Quantitative Raman spectrum and reliable thickness identification for atomic layers on insulating substrates. *ACS Nano* **2012**, *6*, 7381–7388.

[45] Lui, C. H.; Li, Z. Q.; Chen, Z. Y.; Klimov, P. V.; Brus, L. E.; Heinz, T. F. Imaging stacking order in few-layer graphene. *Nano Lett.* **2010**, *11*, 164–169.

[46] Cong, C. X.; Yu, T.; Sato, K.; Shang, J. Z.; Saito, R.; Dresselhaus, G. F.; Dresselhaus, M. S. Raman characterization of ABA- and ABC-stacked trilayer graphene. *ACS Nano* **2011**, *5*, 8760–8768.

[47] Cong, C.; Yu, T.; Saito, R.; Dresselhaus, G. F.; Dresselhaus, M. S. Second-order overtone and combination Raman modes of graphene layers in the range of 1690−2150 $cm^{-1}$. *ACS Nano* **2011**, *5*, 1600–1605.

[48] Li, H.; Lu, G.; Wang, Y. L.; Yin, Z. Y.; Cong, C. X.; He, Q. Y.; Wang, L.; Ding, F.; Yu, T.; Zhang, H. Mechanical exfoliation and characterization of single- and few-layer nanosheets of $WSe_2$, $TaS_2$, and $TaSe_2$. *Small* **2013**, *9*, 1974–1981.

[49] Shi, Y. M.; Dong, X. C.; Chen, P.; Wang, J. L.; Li, L. J. Effective doping of single-layer graphene from underlying $SiO_2$ substrates. *Phys. Rev. B* **2009**, *79*, 115402.

[50] Chakraborty, B.; Bera, A.; Muthu, D. V. S.; Bhowmick, S.; Waghmare, U. V.; Sood, A. K. Symmetry-dependent phonon renormalization in monolayer $MoS_2$ transistor. *Phys. Rev. B* **2012**, *85*, 161403.

[51] Berkdemir, A.; Gutierrez, H. R.; Botello-Mendez, A. R.; Perea-Lopez, N.; Elias, A. L.; Chia, C. I.; Wang, B.; Crespi, V. H.; Lopez-Urias, F.; Charlier, J. C. et al. Identification of individual and few layers of $WS_2$ using Raman spectroscopy. *Sci. Rep.* **2013**, *3*, 1755.

[52] Peimyoo, N.; Yang, W. H.; Shang, J. Z.; Shen, X. N.; Wang, Y. L.; Yu, T. Chemically driven tunable light emission of charged and neutral excitons in monolayer $WS_2$. *ACS Nano* **2014**, *8*, 11320–11329.

[53] Rudin, S.; Reinecke, T. L.; Segall, B. Temperature-dependent exciton linewidths in semiconductors. *Phys. Rev. B* **1990**, *42*, 11218–11231.

[54] Shinada, M.; Sugano, S. Interband optical transitions in extremely anisotropic semiconductors. I. Bound and unbound exciton absorption. *J. Phys. Soc. Jpn.* **1966**, *21*, 1936–1946.

[55] Wang, L. Q.; Kutana, A.; Yakobson, B. I. Many-body and spin-orbit effects on direct-indirect band gap transition of strained monolayer $MoS_2$ and $WS_2$. *Annalen der Physik* **2014**, *526*, L7–L12.

[56] Berkelbach, T. C.; Hybertsen, M. S.; Reichman, D. R. Theory of neutral and charged excitons in monolayer transition metal dichalcogenides. *Phys. Rev. B* **2013**, *88*, 045318.

[57] Najmaei, S.; Liu, Z.; Ajayan, P. M.; Lou, J. Thermal effects on the characteristic Raman spectrum of molybdenum disulfide ($MoS_2$) of varying thicknesses. *Appl. Phys. Lett.* **2012**, *100*, 013106.

[58] Lanzillo, N. A.; Birdwell, A. G.; Amani, M.; Crowne, F. J.; Shah, P. B.; Najmaei, S.; Liu, Z.; Ajayan, P. M.; Lou, J.; Dubey, M. et al. Temperature-dependent phonon shifts in monolayer $MoS_2$. *Appl. Phys. Lett.* **2013**, *103*, 093102.

[59] Peimyoo, N.; Shang, J. Z.; Yang, W. H.; Wang, Y. L.; Cong, C. X.; Yu, T. Thermal conductivity determination of suspended mono- and bilayer $WS_2$ by Raman spectroscopy. *Nano Res.* **2014**, DOI 10.1007/s12274-014-0602-0.

[60] Li, X. S.; Zhu, Y. W.; Cai, W. W.; Borysiak, M.; Han, B. Y.; Chen, D.; Piner, R. D.; Colombo, L.; Ruoff, R. S. Transfer of large-area graphene films for high-performance transparent conductive electrodes. *Nano Lett.* **2009**, *9*, 4359–4363.

[61] Kresse, G.; Furthmüller, J. Efficiency of *ab-initio* total energy calculations for metals and semiconductors using a plane-wave basis set. *Comput. Mater. Sci.* **1996**, *6*, 15–50.

[62] Kresse, G.; Furthmüller, J. Efficient iterative schemes for *ab initio* total-energy calculations using a plane-wave basis set. *Phys. Rev. B* **1996**, *54*, 11169–11186.

[63] Kresse, G.; Joubert, D. From ultrasoft pseudopotentials to the projector augmented-wave method. *Phys. Rev. B* **1999**, *59*, 1758–1775.